Microstructure and Hydrothermal Stability of Microporous Niobia-Silica Membranes: Effect of Niobium Doping Contents

Jiachen Xia [1], Jing Yang [1],*, Hao Zhang [2], Yingming Guo [1] and Ruifeng Zhang [1]

[1] School of Urban Planning and Municipal Engineering, Xi'an Polytechnic University, Xi'an 710048, China; xiajiachen02@163.com (J.X.); guoyingming@xpu.edu.cn (Y.G.); ruifengzhangtry@xpu.edu.cn (R.Z.)

[2] Xi'an Thermal Power Research Institute Co., Ltd., Xi'an 710032, China; zhanghao@mail.tpri.com.cn

* Correspondence: jingy76@163.com

Abstract: Methyl-modified niobium-doped silica (Nb/SiO_2) materials with various Nb/Si molar ratios (n_{Nb}) were fabricated using tetraethoxysilane and methyltriethoxysilane as the silica source and niobium pentachloride as the niobium source by the sol–gel method, and the Nb/SiO_2 membranes were prepared thereof by the dip-coating process under an N_2 calcining atmosphere. Their microstructures were characterized and gas permeances tested. The results showed that the niobium element existed in the formation of the Nb-O groups in the Nb/SiO_2 materials. When the niobium doping content and the calcining temperature were large enough, the Nb_2O_5 crystals could be formed in the SiO_2 frameworks. With the increase of n_{Nb} and calcination temperature, the formed particle sizes increased. The doping of Nb could enhance the H_2/CO_2 and H_2/N_2 permselectivities of SiO_2 membranes. When n_{Nb} was equal to 0.08, the Nb/SiO_2 membrane achieved a maximal H_2 permeance of 4.83×10^{-6} $mol·m^{-2}·Pa^{-1}·s^{-1}$ and H_2/CO_2 permselectivity of 15.49 at 200 °C and 0.1 MPa, which also exhibited great hydrothermal stability and thermal reproducibility.

Keywords: niobium doping; calcination temperature; Nb/SiO_2 membrane; H_2 permselectivities; hydrothermal stability

1. Introduction

Environmental protection and resource shortage are nowadays issues that need to be faced in the process of world development. The continuous growth of the world's population has led to the increasing consumption of the earth's resources. Some experts have suggested hydrogen as an alternative fuel because of its zero pollution. Nowadays, hydrogen is primarily produced from fossil fuels, such as natural gas and coal through steam reforming/gasification and water gas shift reactions [1]. In order to obtain high purity hydrogen from either syngas or the products of the water-gas shift reaction, separation of H_2 from other gases such as CO_2, CO, or CH_4 is necessary. Consequently, hydrogen purification from the above CO_2-containing reaction gas mixture is becoming an important issue. After long-term research and efforts by scientists, a large number of experimental results have shown that the membrane separation technology has shown great potential in gas separation. An inorganic membrane has the advantages of good resistance to high temperature and pressure, high mechanical strength, good chemical stability, long service life, and resistance to halite, which make it attractive in the field of gas separation [2]. In the last two decades, H_2-separation membranes have been developed using various materials, such as palladium and its alloys, silica, alumina, etc. In the research to date, inorganic silica membranes, especially those derived from the sol-gel technique, are some of the best among the various inorganic materials for the separation of hydrogen-containing gas mixtures.

However, in high temperature and humid air, pure SiO_2 membranes showed poor hydrothermal stability. The Si-O-Si bonds were broken and Si-OH bonds were formed when inter-played with water, resulting in the densification of the silica structure [3,4]. Many scientists have carried out a lot of research work to improve the hydrothermal stability of silica

membrane materials. In recent years, the two primary methods have been the introduction of groups such as F^-, Cl^-, $-C_nH_{2n}$, $-C_nH_{2n+1}$, phenyl groups, etc. [5,6], and the doping of transition metals such as nickel [7–9], palladium [10,11], zirconium [12], niobium [13], magnesium [14], aluminum [15], cobalt [16,17], etc. Wei et al. [6] prepared a perfluorodecyl-modified silica membrane by the sol-gel method using tetraethylorthosilicate (TEOS) and 1H, 1H, 2H, and 2H-perflouorodecyltriethoxysilane (PFDTES) as precursors. The H_2 permeance of the as-prepared membrane was 9.71×10^{-7} mol·m^{-2}·s^{-1}·Pa^{-1}, and the H_2/CO_2 permselectivity and binary gas separation factor were 7.19 and 12.11, respectively. Under humid conditions with a temperature of 250 °C and a water vapor molar ratio of 5%, the single H_2 permeance and H_2/CO_2 permselectivity remained almost constant for at least 200 h.

Among the transition metals, niobium doping has caught researchers' eyes. Boffa et al. [18] prepared niobia-silica membranes using tetraethyl orthosilicate (TEOS) as the Si source and niobium penta (n-butoxide) as the Nb source. Their research results showed that the hydrothermal stability of the microporous niobia-silica membranes was better than that of the pure SiO_2 membrane because the incorporation of Nb ions into the silica matrix. Qi et al. [13] prepared a novel microporous hybrid silica membrane using 1,2-bis (triethoxysilyl) ethane (BTESE) and niobium penta (n-butoxide) as precursors for the permselectivity of CO_2. The result showed that the permselectivity of H_2/CO_2 for the Nb-BTESE membrane could be tuned by altering the calcination temperature. Lin et al. [19] investigated the influence of the sol particle size on the gas permselectivity of the niobium-doped hybrid silica membrane. The prepared Nb/SiO_2 membrane had an H_2 permeability of 8.36×10^{-8} mol·m^{-2}·s^{-1}·Pa^{-1} with a mean particle size of 5 nm. However, there have been few studies focusing on the effects of niobium doping content on the microstructures and gas permeances of niobium-doped SiO_2 membranes.

In this work, we prepared a kind of new niobium-doped SiO_2 membrane using tetraethoxysilane (TEOS) and methyltriethoxysilane (MTES) as the Si sources and niobium pentachloride ($NbCl_5$) as the niobium source. Nb/SiO_2 membranes with different Nb/Si molar ratios (n_{Nb}) were prepared. The effects of n_{Nb} and calcination temperature on the microstructures of Nb/SiO_2 materials were studied in detail. Characterization and results were attained by Fourier transform infrared (FTIR) spectroscopy, X-ray diffraction (XRD), X-ray photo electron spectroscopy (XPS), N_2 adsorption/desorption measurements, and scanning electron microscopy (SEM). The gas permeation tests and hydrothermal stability of the Nb/SiO_2 membranes were performed and are discussed.

2. Experimental

2.1. Fabrication of Nb/SiO₂ Sols

The Nb/SiO_2 sols were prepared using tetraethoxysilane (TEOS) and methyltriethoxysilane (MTES) as the silica sources, niobium pentachloride ($NbCl_5$) as the niobium source, absolute ethanol (EtOH) as the solvent, and HCl as the catalyst. High purity solid $NbCl_5$ powder was dissolved in absolute ethanol to obtain a 0.43 M $NbCl_5$ solution. This process was carried out in a fume hood, stirring and dissolving with a glass rod until the HCl gas was released. The reaction equation is as follows:

$$NbCl_5 \text{ (s)} + nC_2H_5OH \text{ (l)} \rightarrow NbCl_{5-n}(OC_2H_5)_n \text{ (l)} + nHCl \text{ (g)}$$

According to the mol ratio of TEOS:MTES:EtOH:H_2O:HCl:$NbCl_5$ = 1:0.8:16:7:0.085:n_{Nb}, the EtOH, TEOS, and MTES were first mixed with the solution of $NbCl_5$ solution in an ice bath and stirred magnetically for 40 min. After that, a mixture of HCl and water was carefully added drop-wise and then refluxed in a water bath at 60 °C for 3 h. In this way, the Nb-doped SiO_2 sols were obtained. The n_{Nb} is the molar ratio of Nb/TEOS, which was 0, 0.08, 0.2, and 1, respectively. The Nb-doped SiO_2 sol with n_{Nb} = 0 is also referred to as the SiO_2 sol. The Nb-doped SiO_2 sols were diluted three times using absolute ethanol to obtain the final Nb/SiO_2 sols.

2.2. Fabrication of Nb/SiO₂ Materials

The as-prepared Nb/SiO₂ sols were dried in a vacuum oven to prepare the dry gels. The obtained dry gels were then ground into fine powders and calcined under N_2 atmosphere in a temperature-controlled tubular furnace at various temperatures (200 °C, 400 °C, 600 °C, 800 °C) for 2 h with a ramping rate of 0.5 °C·min^{-1}. The final niobium-doped silica (Nd/SiO₂) materials were produced. The Nb/SiO₂ materials with $n_{Nb} = 0$ were also referred to as the SiO₂ materials.

2.3. Fabrication of Nb/SiO₂ Membranes

To obtain the Nb/SiO₂ membranes, part of the above Nb/SiO₂ sols were applied to the surface of porous α-Al₂O₃ composite discs (Hefei Shijie Membrane Engineering Co., Ltd., Hefei, China) by the dip-coating method. The discs each had a thickness of 4 mm, a diameter of 30 mm, a mean pore diameter of 100 nm, and a porosity of 40%. The dipping time was 6 s. Four-layer Nb/SiO₂ membranes were prepared, and each Nb/SiO₂ layer was individually calcined under N_2 atmospheres in a temperature-controlled furnace to 400 °C at a ramping rate of 0.5 °C·min^{-1} and with a dwell time of 2 h. The prepared Nb/SiO₂ membranes were used to test the permeances of H_2, CO_2, and N_2; the preparation process is shown in Figure 1.
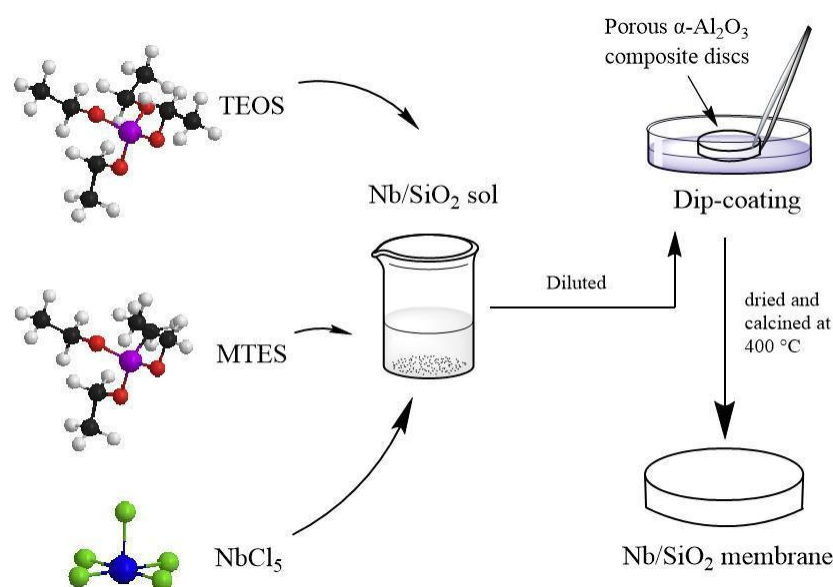
Figure 1. Schematic diagram of the fabrication of Nb/SiO₂ membranes by the sol–gel process.

2.4. Steam-Treatment and Regeneration of Nb/SiO₂ Membranes

The steam stability of the membranes was tested by exposure to saturated steam at 25 °C for 10 d. The thermal regeneration of Nb/SiO₂ membranes after steam treatment was carried out at a calcination temperature of 350 °C by the same calcining procedure as described above. After the steam-treatment and regeneration, the gas permeances of Nb/SiO₂ membranes were tested, respectively.

2.5. Characterization

The sol densities were determined using a pycnometer. The solid contents of sols were determined by the weighing method. The particle size distributions of Nb/SiO₂ sols were measured using a Malvern Nano ZS size analysis instrument (Malvern Instruments Ltd., Malvern, UK) The functional groups of samples were characterized by Fourier transform infrared spectroscopy (FTIR, Nicolet 5700, Thermo Nicolet Corporation, Fitchburg, WI, USA), and the wavelength measurement range was 400–4000 cm^{-1} as determined by the KBr compression method. The material phase structure was determined by a Rigaku D/max-

2550 pc X-ray diffractometer (XRD, Rigaku D/max-2550, Hitachi, Tokyo, Japan) with CuKα radiation under the conditions of 40 kV and 40 mA. The chemical components of Nb/SiO$_2$ samples were performed by an X-ray photoelectron spectrometer (XPS, ESCALAB250xi, Thermo Scientific, Waltham, MA, USA) with AlKα excitation. The morphologies of surfaces and cross-sections for the membranes were observed by scanning electron microscopy (SEM, JEOL JSM-6300, Hitachi, Tokyo, Japan) under 5 kV acceleration voltage. Before the SEM tests, the samples were treated with gold spraying. The BET surface area and pore volume of the samples were measured by N$_2$ sorption/desorption isotherms with a specific surface area and pore and pore-size analyzer (ASAP 2020, Micromeritics, Norcross, GA, USA).

Single gas permeances of Nb/SiO$_2$ membranes were measured under a transmembrane pressure of 0.1-0.4 MPa using the schematic diagram of the experimental setup shown in Figure 2. Prior to the gas permeation measurement, the membranes were mounted in a stainless-steel module with a cylindrical geometry and placed inside the furnace in the gas permeation measurement rig at a temperature range of 25 to 200 °C. The membranes were tested using single gases with different kinetic diameters (H$_2$, CO$_2$, and N$_2$), and permeance was measured by using a soap film flow meter. The gas permselectivities, also known as ideal selectivities, were calculated by the permeance ratio between two gases. The steam stability of the membranes was tested by exposure to saturated steam at 25 °C for 10 d. The thermal regeneration of Nb/SiO$_2$ membranes after steam stability testing was carried out at a calcination temperature of 350 °C by the same calcining procedure as described above. It should also be noted that permeate gas flow was only recorded after a steady state was attained.
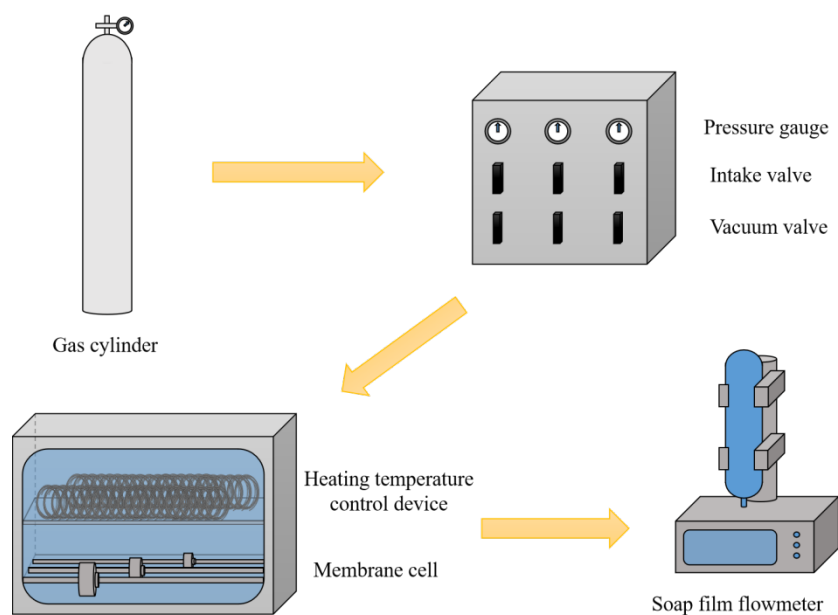
Figure 2. Schematic diagram of the experimental setup.

3. Results and Discussion

3.1. Analysis of Nb/SiO$_2$ Sol Performance

The influence of n$_{Nb}$ on the pH value, density, and solid content of Nb/SiO$_2$ sol is shown in Table 1. The particle size distributions of Nb/SiO$_2$ sols with various n$_{Nb}$ are depicted in Figure 3. As seen in Table 1, with increasing n$_{Nb}$, the sol pH value decreased while the density and solid content increased. As seen in Figure 3, with the increase of n$_{Nb}$, the mean particle sizes of Nb/SiO$_2$ sols increased, and their particle size distributions became wider. The particle size distributions of Nb/SiO$_2$ sols with n$_{Nb}$ = 0, 0.08, and 0.2 were narrow, and their mean particle sizes were small. However, when n$_{Nb}$ was increased to 1.0, the mean particle size of Nb/SiO$_2$ sol increased greatly. In the experiment, the prepared

NbCl$_5$ solution was acidic. The increase of n_{Nb} in Nb/SiO$_2$ sol made the acidity of the sol increase, which sped up the hydrolysis–polycondensation reaction. As a result, the sol density, solid content, and particle size increased. On the other hand, with the occurrence of the hydrolysis-polycondensation reaction, Nb-O-Si bonds were formed gradually. The radius of the niobium atom (2.08 Å) is larger than that of the Si atom (1.46 Å), and the bond length of Nb-O is longer than that of Si-O (the bond lengths of Nb-O and Si-O are about 2.13 and 1.64 Å, respectively), which contributed to the increase of sol particles.

Table 1. The influence of n_{Nb} on the pH value, density, and solid content of Nb/SiO$_2$ sol.

n_{Nb}	pH	Density/g·cm^{-3}	Solid Content/%
0	3.41 ± 0.04	0.8418 ± 0.0007	22.31 ± 0.04
0.08	2.93 ± 0.03	0.8529 ± 0.0006	22.58 ± 0.05
0.2	2.64 ± 0.02	0.8710 ± 0.0008	22.80 ± 0.06
1	1.02 ± 0.02	0.9130 ± 0.0006	24.46 ± 0.07
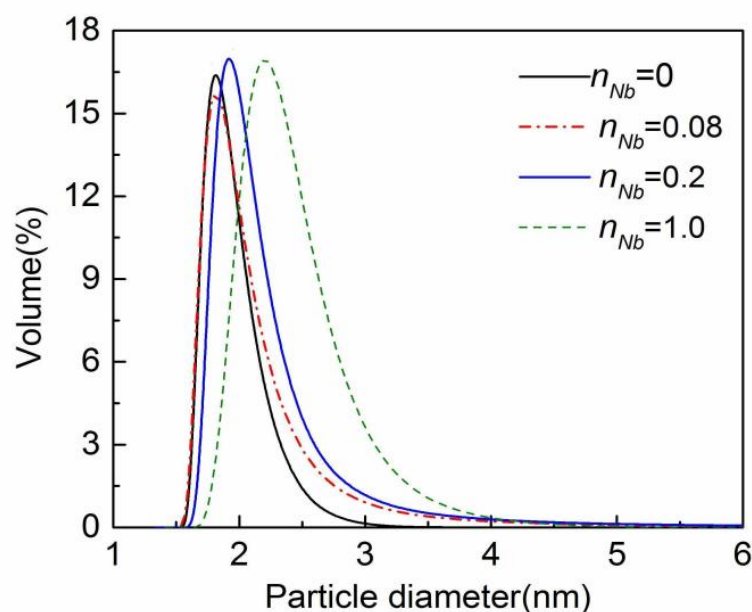
Figure 3. The particle size distributions of Nb/SiO$_2$ sols with various n_{Nb}.

3.2. Chemical Structure Analysis

The phase-chemical structure of Nb/SiO$_2$ materials may be influenced by the introduced Nb element, so that the effect may have been more evident in the samples containing higher Nb contents. In order to study the effect of calcination temperature on Nb/SiO$_2$ materials, the Nb/SiO$_2$ samples with n_{Nb} = 1 were used for the measurement analysis. Figure 4 shows the FTIR spectra of Nb/SiO$_2$ materials with n_{Nb} = 1 at different calcination temperatures. In Figure 4, the absorption peaks located at 1055 and 788 cm^{-1} were associated with the Si-O-Si bonds. The peaks at 2985 cm^{-1} and 1630 cm^{-1} were assigned to the mode of -CH$_3$ groups and Si-OH bonds, respectively [11]. The band at 1278 cm^{-1} was designated as Si-CH$_3$ groups. The intensity of the absorption peaks at 2985 cm^{-1} and 1278 cm^{-1} decreased obviously with increases in the calcination temperatures and disappeared as the calcination temperature reached 600 °C, indicating that the -CH$_3$ groups had been broken down at this temperature. The absorption peak observed at 619 cm^{-1} corresponded to the Nb-O bonds, which enhanced in intensity with the increase of calcination temperatures.
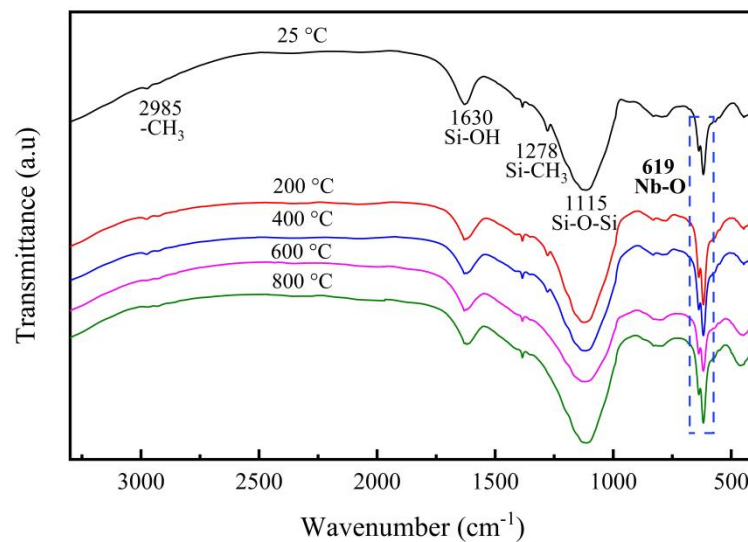
Figure 4. FTIR spectra of Nb/SiO_2 materials with $n_{Nb} = 1$ calcined at various temperatures.

The FTIR spectra of Nb/SiO_2 materials with various n_{Nb} calcined at 400 °C are provided in Figure 5. It can be seen from Figure 5 that the hydrophobic $Si-CH_3$ groups located at 1278 cm^{-1} were all involved in the Nb/SiO_2 materials with various n_{Nb}. The absorption peak locations of Nb/SiO_2 materials with $n_{Nb} = 0.08$, 0.2, and 1 were roughly the same, but the intensities of individual peaks were different. The peak located at 619 cm^{-1} corresponding to the Nb-O groups did not exist in the pure SiO_2 materials. This certified that the Nb had been successfully incorporated into the silica frameworks. At the same time, the peak intensity due to the Nb-O groups became strong continuously with the increase of niobium doping.
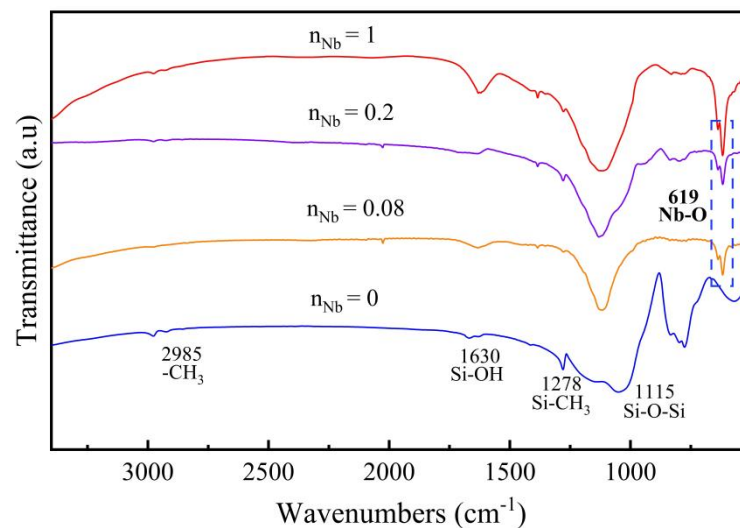
Figure 5. FTIR spectra of Nb/SiO_2 materials with various n_{Nb} calcined at 400 °C.

3.3. Phase Structure Analysis

The XRD patterns of Nb/SiO_2 materials with $n_{Nb} = 1$ calcined at various temperatures are given in Figure 6. The broad diffraction peak at the range of about $2\theta = 20$–30° was assigned to the amorphous SiO_2. An obvious crystallization peak of Nb_2O_5 was detected when the calcination temperature was increased to 600 °C. According to the conclusion from Kosutova, there will be two new crystalline phases formed sequentially when the sample is heated up to 450 °C [20]. The first crystalline phase was identified as hexagonal TT-Nb_2O_5 (JCPDS No-400-028-0317) [21]. The TT notation comes from the German Tief-Tief

(low–low), referring to the temperature at which the structure was observed in the sequence of niobium oxides obtained at elevated temperatures, first used in Ref [22]. In Figure 6, the diffraction peaks at $2\theta = 22.6°, 28.6°, 36.8°, 46.2°, 50.8°$, and $55.2°$ were assigned to the (001), (180), (201), (002), (380), and (182) crystal planes, respectively, of hexagonal TT-Nb_2O_5, which indicated the formation of hexagonal TT-Nb_2O_5 (JCPDS No.00-030-0873). In Figure 6, another phase transition was observed at 800 °C, which was associated with the transition from hexagonal TT-Nb_2O_5 to orthorhombic T-Nb_2O_5 (JCPDS No. 404-007-0752) [23]. The transformation caused the splitting of the diffraction peaks [24]. It is evident that a high calcining temperature can improve the crystallinity of Nb_2O_5 species.
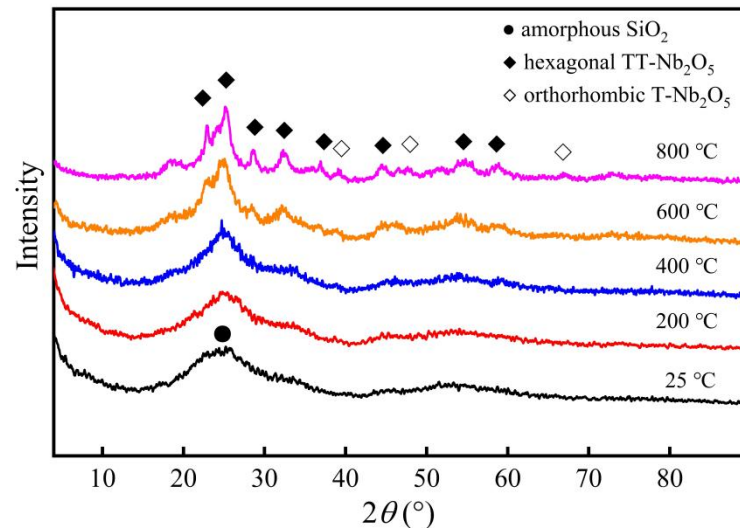
Figure 6. XRD patterns of Nb/SiO_2 materials with $n_{Nb} = 1$ calcination at various temperatures.

The XRD patterns of the Nb/SiO_2 materials with various n_{Nb} calcined at 400 °C are provided in Figure 7. From Figure 7, it can be seen that as the $n_{Nb} \leq 0.2$, the XRD curves of the Nb/SiO_2 materials were similar, and only the diffraction peak between 20° and 30° corresponding to the amorphous SiO_2 could be observed. When the n_{Nb} was increased to 1, a new diffraction peak assigned to the hexagonal TT-Nb_2O_5 appeared besides for the amorphous SiO_2. This means there was no crystalline form of hexagonal TT-Nb_2O_5 when the Nb-doped content was low. When the niobium doping content and the calcining temperature were large enough, the Nb_2O_5 crystals could be formed in the SiO_2 frameworks.
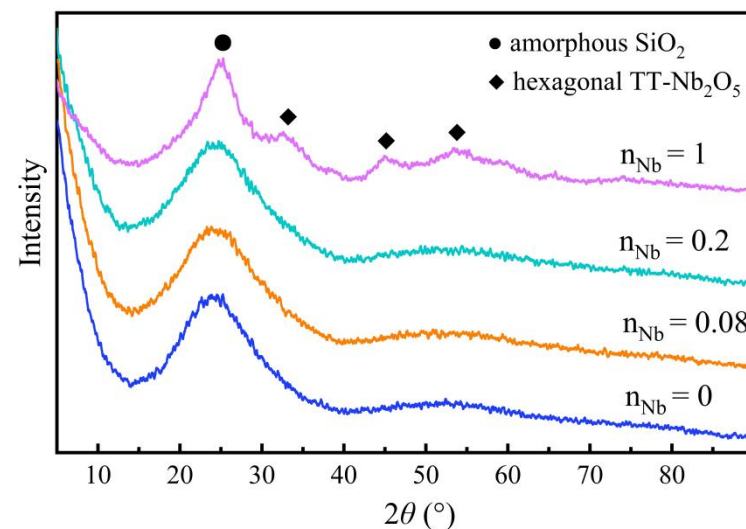
Figure 7. XRD patterns of Nb/SiO_2 materials doped with various n_{Nb} calcined at 400 °C.

In order to explore the crystal form of niobium, the Nb/SiO_2 materials with n_{Nb} = 1 calcined at various temperatures were characterized by XPS, which are shown in Figure 8. In Figure 8, the Nb^{TT} 3d and Nb^T 3d mean the Nb-O of the hexagonal crystal system TT-Nb_2O_5 and orthorhombic crystal system T-Nb_2O_5, respectively. It can be seen that the Nb^{TT} $3d_{5/2}$ peak and the Nb^{TT} $3d_{3/2}$ peak appeared at 206.4 eV and 209.1 eV, respectively, in the sample calcined at 400 °C. The data matched with the species of niobium oxide, which proved the formation of Nb_2O_5 crystals. The temperature related to the formation of the TT-Nb_2O_5 phase was reported to be approximately 500 °C or higher, according to the studies conducted on nanostructures or thin films [24,25]. Furthermore, the calcination temperature reached 600 °C, and the Nb^T $3d_{5/2}$ and Nb^T $3d_{3/2}$ peaks also appeared at 209.0 eV and 211.8 eV, respectively, which were the Nb 3d peaks of orthorhombic phase T-Nb_2O_5. The conclusion was as same as that of XRD analysis.
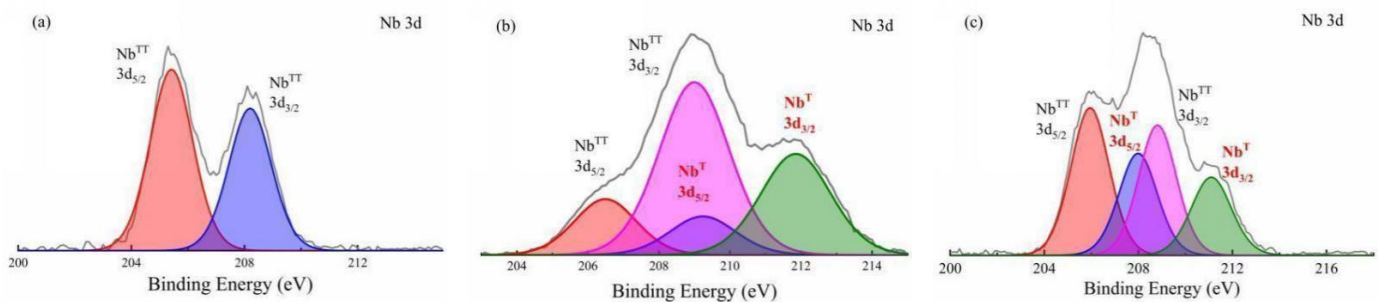
Figure 8. The Nb 3d XPS patterns of Nb/SiO_2 materials with n_{Nb} = 1 calcined at various temperatures: (**a**) 400 °C, (**b**) 600 °C, and (**c**) 800 °C.

3.4. SEM Analysis

Figure 9 shows the SEM images of Nb/SiO_2 materials with various n_{Nb} calcined at various temperatures. From Figure 9a–d, it can be seen that when calcined at 400 °C, the samples had the morphology of nanoparticles with dispersed amorphous structures, and the particle sizes increased with increasing n_{Nb}.
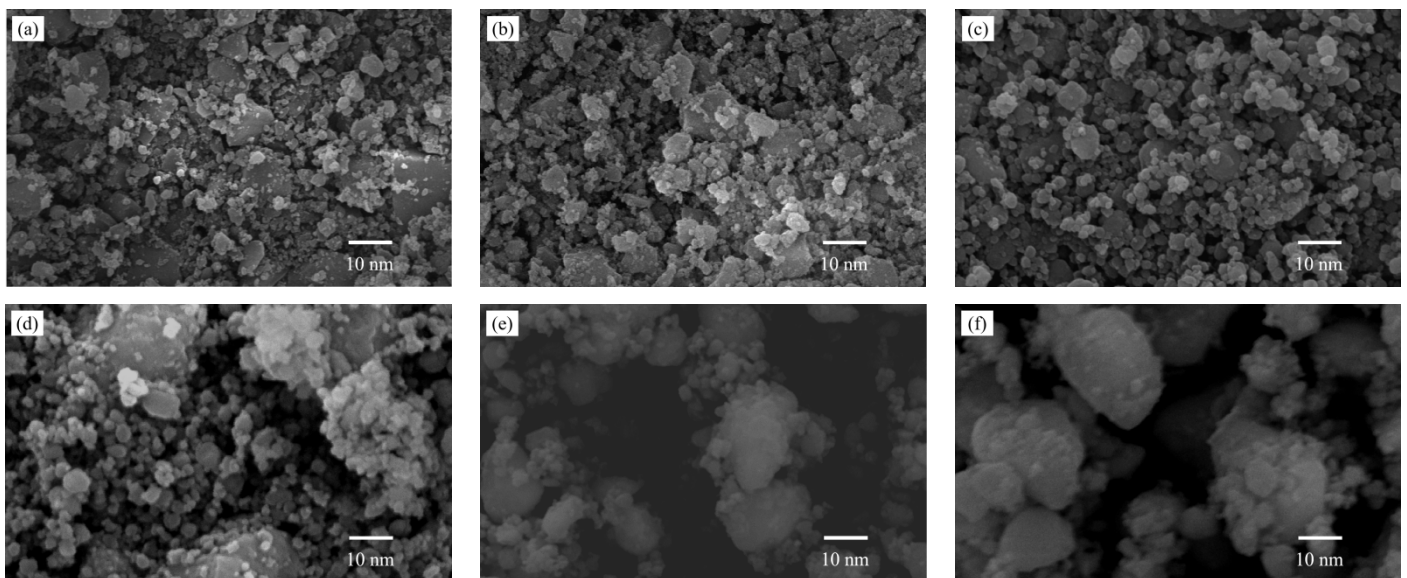
Figure 9. SEM image of Nb/SiO_2 materials with various n_{Nb} calcinations at various temperatures: (**a**) n_{Nb} = 0, 400 °C; (**b**) n_{Nb} = 0.08, 400 °C; (**c**) n_{Nb} = 0.2, 400 °C; (**d**) n_{Nb} = 1, 400 °C; (**e**) n_{Nb} = 1, 600 °C; (**f**) n_{Nb} = 1, 800 °C.

Comparing Figure 9d with Figure 9e,f, it can be clearly observed that the morphology and particle size of Nb/SiO_2 material with n_{Nb} = 1 underwent a large change after being

calcined at 600 °C, and the materials had a tendency to develop from an amorphous state to a spherical shape. It can be seen from Figure 9f that when the calcination temperature reached 800 °C, the materials exhibited a spherical structure, the particle size increased, and there were more small-sized spherical particles formed around the large particles. In summary, with the increase of calcination temperature and Nb-doping, the particle sizes increased.

Moreover, the SEM images of the pure SiO_2 membrane and Nb/SiO_2 with $n_{Nb} = 0.08$ calcined at 400 °C are depicted in Figure 10. From Figure 10 it can be observed that there were no visible cracks or pinholes on the membrane surfaces, indicating that the membranes were well coated. It could be seen that niobium doping could make particle sizes increase.
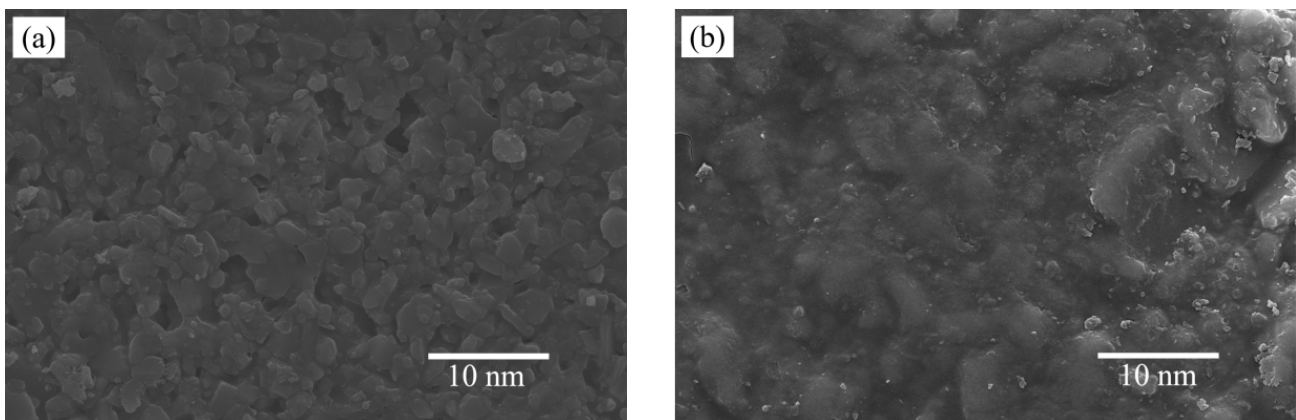
Figure 10. SEM image of Nb/SiO_2 membranes with n_{Nb} = (**a**) 0 and (**b**) 0.08 calcined at 400 °C.

3.5. Pore Structure Analysis

The pore properties of the as-prepared Nb/SiO_2 materials were investigated by N_2 adsorption/desorption to characterize the surface area, pore volume, and porosity. Figure 11 shows the N_2 adsorption/desorption isotherms of Nb/SiO_2 materials with various n_{Nb} calcined at 400 °C under an N_2 atmosphere. After calcining, all isotherms displayed similar tendencies, which were similar to a tape I isotherm. It could be proved that the Nb/SiO_2 materials all exhibited the adsorption isotherm characteristics of microporous materials. This material was subjected to a strong force due to the gas in the micropores, so it could quickly reach the absorption saturation state.
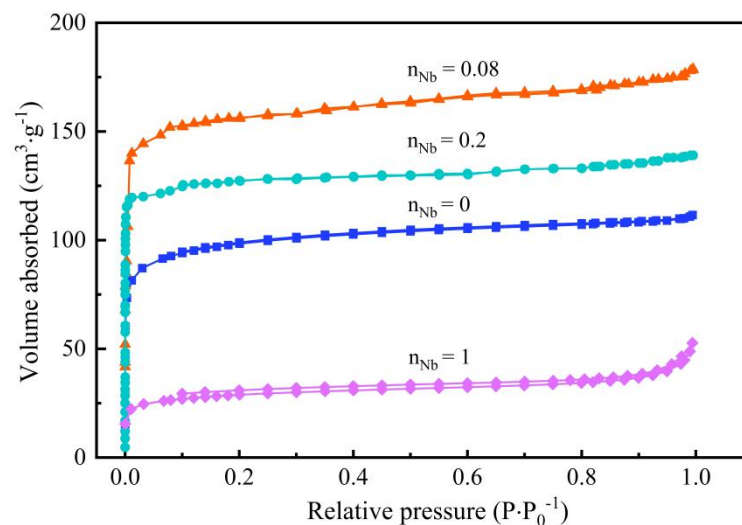
Figure 11. N_2 adsorption–desorption isotherms of Nb/SiO_2 materials doped with various n_{Nb} calcined at 400 °C.

Figure 12 manifests the pore size distribution of Nb/SiO$_2$ materials with various n$_{Nb}$ calcined at 400 °C. As shown in Figure 12, as n$_{Nb}$ ≤ 0.2, with the Nb doping, the pore size of Nb/SiO$_2$ materials were widened, and the microporous structure was maintained. When n$_{Nb}$ = 1, the Nb/SiO$_2$ material became dense.
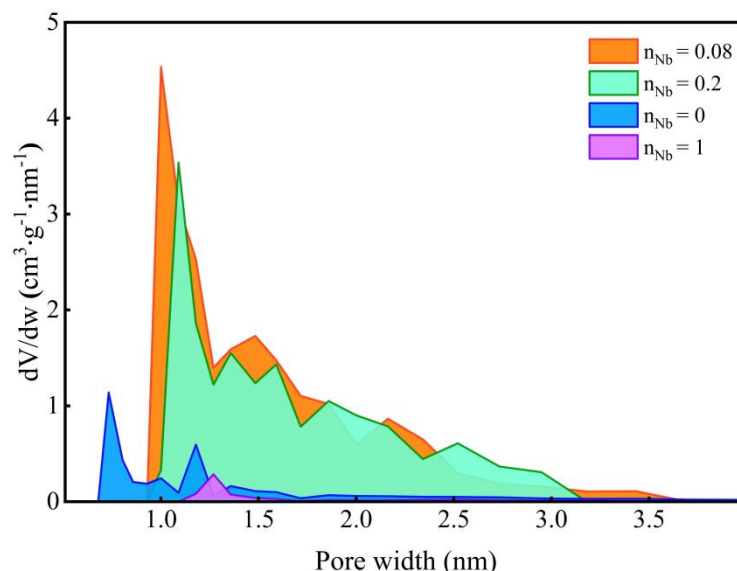
Figure 12. Pore size distribution of Nb/SiO$_2$ materials doped with various n$_{Nb}$ calcined at 400 °C.

The pore structure parameters of Nb/SiO$_2$ materials with various n$_{Nb}$ calcined at 400 °C are shown in Table 2. It can be observed that with the increases of n$_{Nb}$, the mean pore size, BET surface area, and total pore volume increased until n$_{Nb}$ = 0.08, and then they began to decrease. This is because the bond length of Nb-O is longer than that of Si-O (the bond lengths of Nb-O and Si-O are about 2.13 and 1.64 Å, respectively). The formation of the Nb-O bond helped the formation of larger particles. Thus, with the increase of the Nb doping amount, the particle size increased, and the formed pore grew gradually. However, when n$_{Nb}$ was >0.08, that changed. Some small hexagonal TT-Nb$_2$O$_5$ particles were formed and distributed in the SiO$_2$ network, which led to a decrease in the mean pore size, BET surface area, and total pore volume

Table 2. Pore structure parameters of Nb/SiO$_2$ materials with various n$_{Nb}$ calcined at 400 °C.

n$_{Nb}$	BET/ m^2·g^{-1}	V$_t$/ cm^3·g^{-1}	V$_{mic}$/ cm^3·g^{-1}	Mean Pore Width/nm
0	386.4545	0.1716	0.1115	1.8759
0.08	778.7121	0.4901	0.0867	2.4549
0.2	535.4072	0.4632	0.0748	2.2591
1	86.1599	0.0762	0.0266	1.2176

3.6. Gas Permeation and Separation Property Analysis

Based on all the results of the above, the Nb-doping content showed a significant impact on the microstructures of Nb/SiO$_2$ materials. Compared with the Nb/SiO$_2$ membrane with n$_{Nb}$ = 0.08 and n$_{Nb}$ = 0.2, the pore volume of the Nb/SiO$_2$ membrane with n$_{Nb}$ = 1 was too small, which is bad for gas separation. Therefore, the Nb/SiO$_2$ membrane with n$_{Nb}$ = 1 was not considered here.

A transient test was conducted on the Nb/SiO$_2$ membranes with various n$_{Nb}$ at 25 °C and a differential pressure of around 0.1 MPa, and the gas permeances and H$_2$ permselectivities are shown in Figure 13. In Figure 13a, the H$_2$ and N$_2$ permeances of Nb/SiO$_2$ membranes with n$_{Nb}$ = 0.08 and 0.2 were greater than those of the pure SiO$_2$ membrane, while the change trends of CO$_2$ permeances were the contrary. Compared with the pure SiO$_2$ membrane, the H$_2$ permeances of Nb/SiO$_2$ membranes with n$_{Nb}$ = 0.08 and 0.2 in-

creased by 39.0% and 8.9%, respectively. In Figure 13b, the permselectivities of H_2/CO_2 and H_2/N_2 for the pure SiO_2 membrane were greater than the values based on Knudsen diffusion (4.69 and 3.74, respectively), which means the transport in pure SiO_2 membrane is controlled by molecular sieving plus Knudsen diffusion. The H_2/CO_2 and H_2/N_2 permselectivities for the Nb/SiO_2 membranes with n_{Nb} = 0.08 and 0.2, respectively, were obviously higher than those of the pure SiO_2 membrane. Compared with the pure SiO_2 membrane, the H_2/CO_2 permselectivity for the Nb/SiO_2 membranes with n_{Nb} = 0.08 and 0.2 increased by 59.5% and 6.3%, respectively. The larger mean pore size and higher pore volume of Nb/SiO_2 membranes with n_{Nb} = 0.08 and 0.2 than those of the SiO_2 membrane can explain the increase of gas permeance. The larger mean pore size of Nb/SiO_2 membrane indicated that the increase of H_2/CO_2 permselectivity was not due to molecular sieving. This suggests that the doping of Nb introduced another transport mechanism. Some researchers have proposed that doping transition metals into the microporous SiO_2 network will generate Lewis acids on the surface of the membrane materials and ultimately endow the Nb/SiO_2-derived microporous membrane with sufficiently high H_2/CO_2 permselectivity. The exceptionally low permeance of CO_2 is explained as a consequence of strong chemical interactions between CO_2 and the materials of the membrane pore surface, presumably Nb-bound hydroxy groups. The results indicate that the H_2/CO_2 separation was based on sorption rather than on the differences in molecular sizes [26]. In other words, the existence of acid sites on the surface of membranes may play a key role in reducing CO_2 permeance. The H_2/CO_2 and H_2/N_2 permselectivities of the Nb/SiO_2 membrane with n_{Nb} = 0.08 obtained the maximum. Furthermore, with the further increase of n_{Nb}, although there are still acid sites in the membrane materials, the formed Nb_2O_5 in the high-content Nb/SiO_2 materials agglomerates to form a non-selective interfacial gap, which will lead to the densification of the membrane materials [13]. Thereby the average pore size will become smaller, resulting in the decrease of gas permeances and H_2 permselectivities of the Nb/SiO_2 membrane.
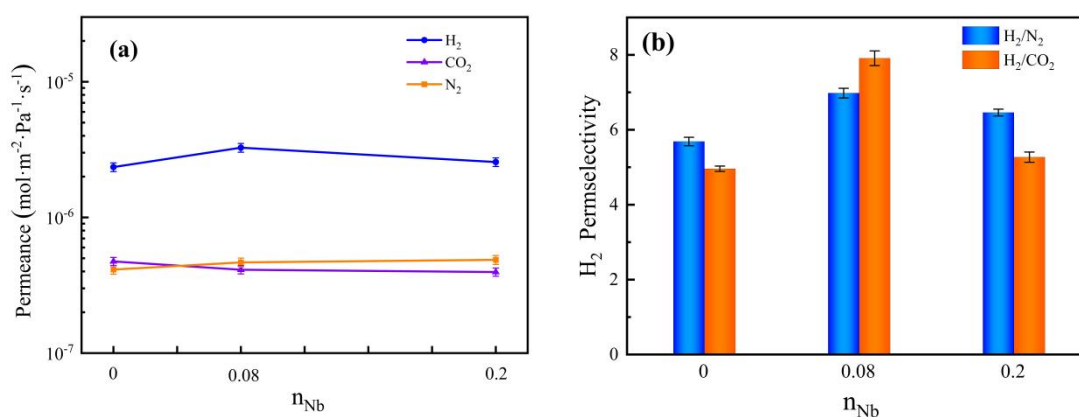
Figure 13. Effect of n_{Nb} on (**a**) gas permeance and (**b**) H_2 permselectivity of Nb/SiO_2 membrane at a pressure difference of 0.1 MPa and 25 °C.

Figure 14 displays the influence of temperature differences on the gas permeance of the Nb/SiO_2 membrane with various n_{Nb} at a pressure difference of 0.1 MPa. As shown in Figure 14, the H_2 permeance and H_2/CO_2 permselectivities in the Nb/SiO_2 membranes with different n_{Nb} revealed an upward trend with increasing temperature when maintaining a constant pressure difference of 0.1 MPa, which indicated that the transport of H_2 molecules through the membranes was activated.

The permeance and permselectivity of the Nb/SiO_2 membrane with n_{Nb} = 0.08 at a pressure difference of 0.1 MPa and temperature change from 25 °C to 200 °C are manifested in Figure 15. It can be clearly seen that H_2 permeance was significantly enhanced with increasing temperature, and the other permeances of CO_2 and N_2 were reduced slightly. The results were the same as the temperature dependency of permeance of several gases in

the NS (Nb/SiO$_2$) membrane from Boffa [27]. Thus, this gives rise to the permselectivity of H$_2$/CO$_2$ and H$_2$/N$_2$ elevating with increasing temperature. With increasing temperatures, the H$_2$ permeance of the Nb/SiO$_2$ membrane increased gradually, which shows that the permeation behavior of H$_2$ in the membranes mainly follows an activation–diffusion mechanism. In the case of activated diffusion, molecules penetrate through the micropore while being subjected to a repulsive force from the pore walls, and the molecules with sufficient kinetic energy to overcome the repulsive force can penetrate the pores [16]. Conversely, the permeance of CO$_2$ and N$_2$ decreased slightly, similar to the trend of Knudsen diffusion, in which molecules collide with the pore walls more regularly than permeating molecules.
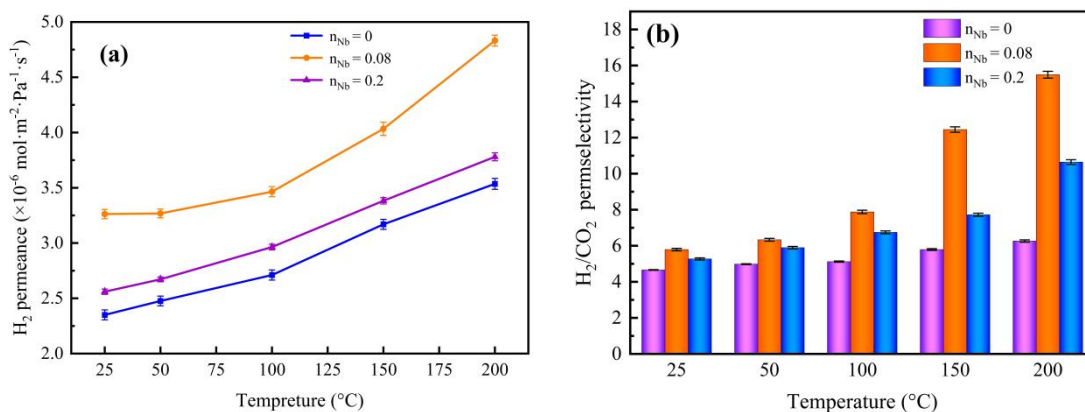
Figure 14. Effect of temperature on (**a**) H$_2$ permeance and (**b**) H$_2$/CO$_2$ permselectivity of Nb/SiO$_2$ membranes with different n_{Nb} at a pressure difference of 0.1 MPa.
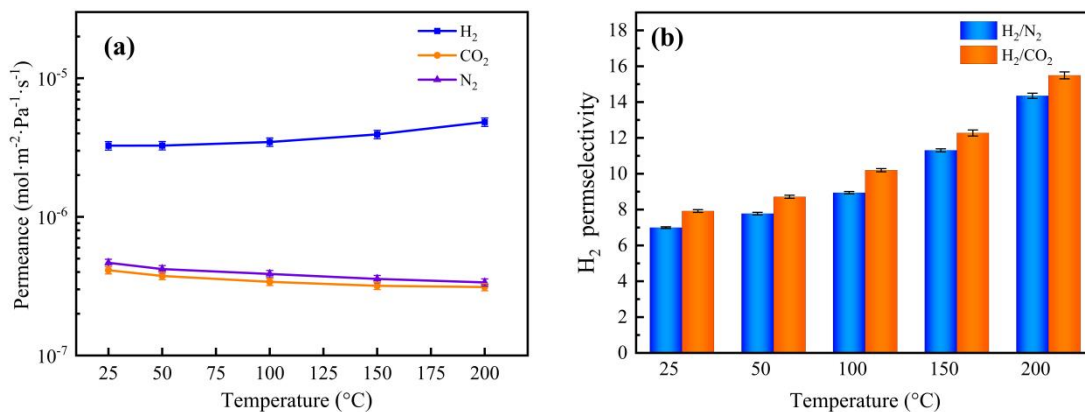
Figure 15. Effect of temperature on (**a**) gas permeance and (**b**) H$_2$ permselectivity of Nb/SiO$_2$ membrane with n_{Nb} = 0.08 at a pressure difference of 0.1 MPa.

After the previous discussion, we believe that the permselectivity of Nb/SiO$_2$ membranes has a sorption separation mechanism. High temperature is conducive to the permselectivity of H$_2$, indicating that the permselectivity mechanism of H$_2$ to other gases is mainly dominated by activation diffusion, which follows the Arrhenius equation.

$$F = A_0 \exp\left(\frac{-E_a}{RT}\right) \tag{1}$$

In the formula, F means permeance, A$_0$ means former factor, E$_\alpha$ means apparent activation energy, R means the ideal gas constant, T means the temperature, and Equation (1) can be described in another form:

$$\ln F = \ln A_0 - \frac{E_a}{RT} = A - \frac{E_a}{RT} \tag{2}$$

The $1/T$ is used as the abscissa and $\ln F$ as the ordinate to draw the graph. It can be seen from the above formula that it is a straight line in theory. The apparent activation energy can be calculated from the slope of the straight line. Then the Arrhenius curves of the three gases are shown in Figure 16. Moreover, from the slope of the straight-line fitting in Figure 16, the apparent activation energy of the three gases can be obtained: $E_m = E_a + Q_{st}$ [28]. The results are shown in Table 4.
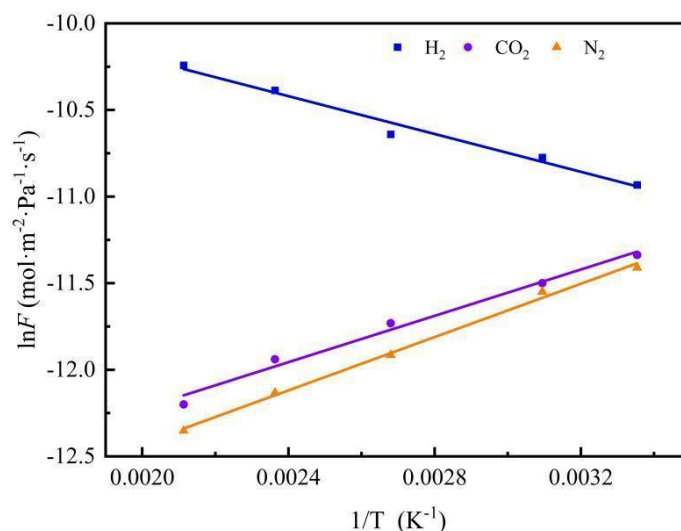
Figure 16. Arrhenius plots of gas (H_2, CO_2, and N_2) permeances in Nb/SiO_2 membrane with $n_{Nb} = 0.08$ at a pressure difference of 0.1 MPa.

From Table 3, Q_{st} means isoteric heat of adsorption, CO_2 exhibits a greater adsorption heat, and the gas with the lowest adsorption heat is H_2. The apparent activation energy (E_a) can be positive or negative, depending on their relative magnitudes. A negative value of E_a is generally interpreted as being caused by strong sorption of the molecule on the pore surface. Such a negative value suggests a high enthalpy of sorption [26]. The mobility energy (E_m) of gas molecules moving on the surface of the Nb/SiO_2 membrane was E_m (CO_2) > E_m (N_2) > E_m (H_2). The permselectivity of the Nb/SiO_2 membrane towards H_2/CO_2 increased rapidly as a function of temperature. This was probably a result of the high activation energy of the mobility of hydrogen and the high heat of sorption of carbon dioxide. This result has never been reported for pure silica [29–32]. Thus, the strong heat of adsorption should be related to the presence of Nb ions in the microporous framework. Table 4 shows the E_a value of H_2, H_2 permeance, H_2 permselectivities, and mean pore diameter of silica membranes by the sol–gel method from other researchers. From Table 4, it can be observed that it is difficult to improve the H_2 permeance and permselectivity at the same time. In addition, a higher E_a always corresponds to a smaller mean pore diameter and lower H_2 permeance. This means that the E_a value maybe have a link with the mean pore diameter and the interplay between the molecules of H_2 and the pore walls of the membrane. Therefore, compared with other research groups, the Nb-doping in this work may be the reason for the lower E_a value of H_2.

Table 3. E_a, Q_{st}, and E_m values of gases (H_2, CO_2, and N_2) calculated from the Arrhenius formula for the Nb/SiO_2 membrane with $n_{Nb} = 0.08$ at a pressure difference of 0.1 MPa.

Gases	E_a/ kJ·mol^{-1}	Q_{st}/ kJ·mol^{-1} [28]	E_m/ kJ·mol^{-1}
H_2	2.53	6	8.53
CO_2	−4.28	24	19.72
N_2	−4.07	18	13.93

Table 4. E_a of H_2, H_2 permeances, H_2 permselectivities, and mean pore diameter for various SiO_2 membranes prepared by other researchers using the sol–gel process.

Membrane Type	Temperature and Pressure	E_a of H_2 (kJ·mol^{-1})	H_2 Permeance (mol·m^{-2}·Pa^{-1}·s^{-1})	H_2 Permselectivities		Mean Pore Diameter (nm)	Ref.
				H_2/CO_2	H_2/N_2		
SiO_2	200 °C, 2 bar	-	4.62×10^{-7}	3.7	10.5	0.30–0.54	[33]
SiO_2(400)	200 °C, 1 bar	8	17.4×10^{-7}	7.5	64	0.38–0.55	[28]
SiO_2(600)	200 °C, 2 bar	7.6	4.03×10^{-7}	66	-	0.36–0.38	[28]
Pd/SiO_2	200 °C, 0.3 MPa	-	7.26×10^{-7}	4.3	14	0.57	[34]
Co/SiO_2	200 °C, 0.2 MPa	1.98	1.97×10^{-5}	10.48	13.08	2.34	[35]
Nb/SiO_2 *	200 °C, 0.1 MPa	2.53	4.83×10^{-6}	15.49	9.54	2.4549	

* In this work.

The pressure dependence of various gas permeances and H_2/CO_2 permselectivities in the pure SiO_2 membrane and Nb/SiO_2 membrane with various n_{Nb} at 200 °C were further investigated in the pressure difference range from 0.10 MPa to 0.40 MPa, which is shown in Figure 17. It could be observed that H_2 permeance with various n_{Nb} increased with the pressure-dependence increase. This is because the pressure difference elevated, and the gas force increased, resulting in an elevation in the gas concentration in the membrane, and then leading to higher H_2 permeance. As seen in Figure 17b, the permselectivity of H_2/CO_2 changed slightly with increases in the pressure difference.
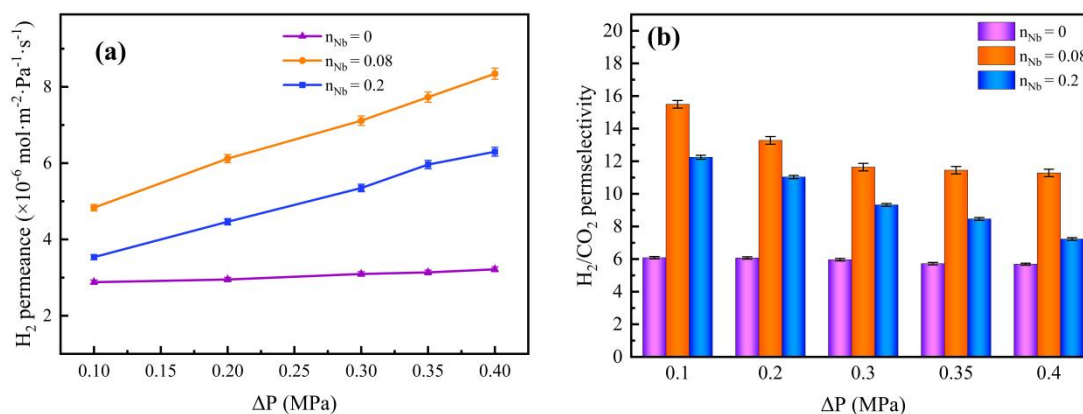
Figure 17. Effect of pressure difference on (**a**) H_2 permeance and (**b**) H_2/CO_2 permselectivity of Nb/SiO_2 membranes with different n_{Nb} at 200 °C.

Figure 18 demonstrates the effect of pressure differences on the permeance and permselectivity of different gases for the Nb/SiO_2 membrane with $n_{Nb} = 0.08$ and a temperature at 200 °C. As seen in Figure 18a, as the pressure difference increased from 0.10 to 0.40 MPa, all of the gas permeances increased. The reason is that the increases in intake pressure resulted in an elevation of the gas concentration, thus yielding a higher permeance. Furthermore, the relationship between permselectivity and pressure differences is shown in Figure 18b. For example, with the pressure increasing from 0.10 MPa to 0.40 MPa, the permeance of N_2 and CO_2 slightly increased. This was due to the small influence of pressure on Knudsen diffusion, as previously reported in the literature [30]. Hence, no matter how high the pressure was, the change in permselectivity would not increase significantly.

Traditional SiO_2 membranes have poor hydrothermal stability due to a large amount of Si-OH groups on their surfaces, which easily absorb water vapor in the air. In the Nb/SiO_2 membrane, not only the Nb-doping but also the introduced hydrophobic groups can improve the vapor stability, which can reduce the hydroxyl groups on the pore surface and enhance the hydrophobicity. In order to test the hydrothermal stability of membranes, the Nb/SiO_2 membranes with $n_{Nb} = 0$ and 0.08 were chosen to investigate the gas permeance before and after steam treatment.
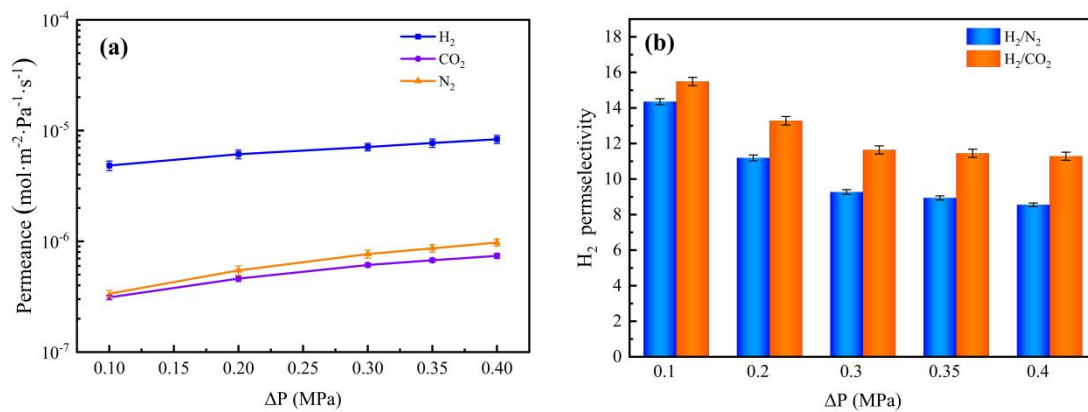
Figure 18. Effect of pressure difference on (**a**) gas permeances and (**b**) H_2 permselectivities of Nb/SiO_2 membrane at 200 °C.

Figure 19 shows the permeances of various gases (H_2, CO_2, and N_2) and H_2 permselectivities of Nb/SiO_2 membranes with n_{Nb} = 0 and 0.08 at 25 °C and a pressure difference of 0.1 MPa before and after steam treatment and regeneration. As shown in Figure 19, compared with the fresh membranes, the H_2 permeances of SiO_2 and Nb/SiO_2 membranes after steam treatment decreased by 17.90% and 6.68%, respectively, while their H_2/CO_2 permselectivities decreased by 3.2% and increased by 1.6%, respectively. After regeneration by calcination at 350 °C, the gas permeances and the permselectivities of H_2/CO_2 and H_2/N_2 for the two membranes showed an upward trend. Compared with the fresh membranes, the H_2 permeances of SiO_2 and Nb/SiO_2 membranes after regeneration decreased by 10.95% and 3.21%, respectively, while their H_2/CO_2 permselectivities increased by 2.8% and 2.1%, respectively. The above results indicate that niobium doping improves the hydrothermal stability of SiO_2 membranes.
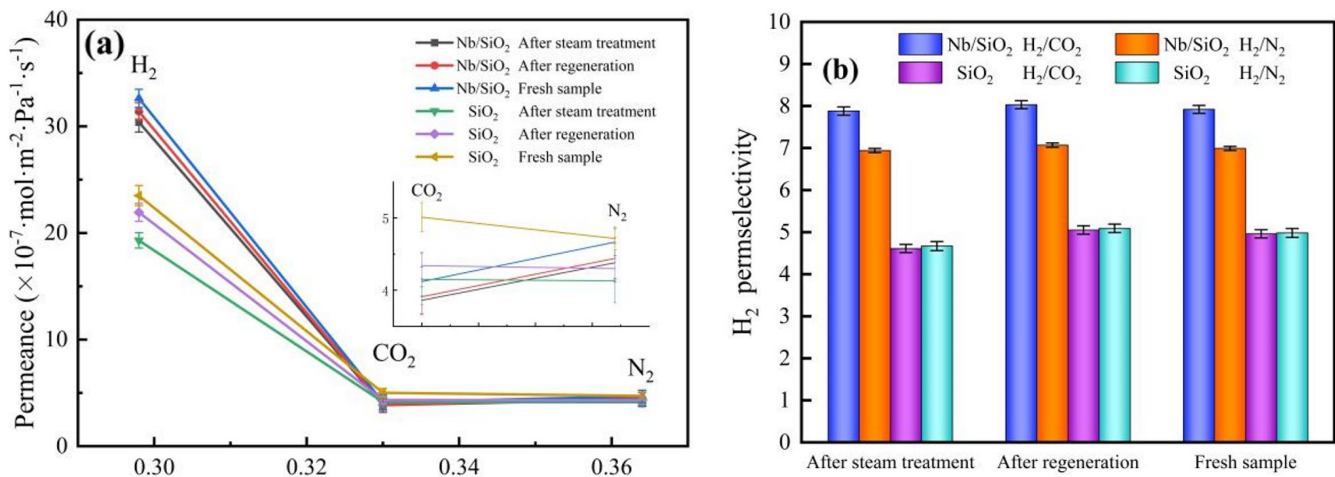
Figure 19. (**a**) Gas permeance and H_2 permselectivities and (**b**) H_2 permselectivities of Nb/SiO_2 membranes with n_{Nb} = 0 and 0.08 at a pressure difference of 0.1 MPa before and after steam treatment and regeneration.

4. Conclusions

To sum up, using the sol-gel technique, Nb/SiO_2 materials and membranes with various n_{Nb} were successfully synthesized. Their microstructures and gas permeances were investigated. The results showed that the niobium element existed in the formation of the Nb-O groups in the Nb/SiO_2 materials. As the niobium doping content and the calcining temperature were high enough, the Nb_2O_5 crystals could be formed in the SiO_2 frameworks. With the increase of n_{Nb}, the formed particle sizes increased, and the mean

pore size, BET surface area, and total pore volume also increased until n_{Nb} = 0.08, and then they began to decrease. The doping of Nb could enhance the H_2/CO_2 and H_2/N_2 permselectivities of the SiO_2 membrane. When n_{Nb} was equal to 0.08, the Nb/SiO_2 membrane achieved a maximal H_2 permeance of 4.83×10^{-6} mol·m^{-2}·Pa^{-1}·s^{-1} and H_2/CO_2 permselectivity of 15.49 at 200 °C and 0.1MPa, which increased by 36.7% and 155.47%, respectively, compared with that of the pure SiO_2 membrane. Compared with the fresh membranes, the H_2 permeances of SiO_2 and Nb/SiO_2 membranes after steam treatment decreased by 17.90% and 6.68%, respectively, while their H_2/CO_2 permselectivities decreased by 3.2% and increased by 1.6%, respectively. After regeneration, the gas permeances and the permselectivities of H_2/CO_2 and H_2/N_2 for the two membranes showed an upward trend. Compared with the fresh membrane, the H_2 permeances of SiO_2 and Nb/SiO_2 membranes after regeneration decreased by 10.95% and 3.21%, respectively, while their H_2/CO_2 permselectivities increased by 2.8% and 2.1%, respectively. Niobium doping improved the hydrothermal stability of the SiO_2 membrane. The Nb/SiO_2 membranes also exhibited great thermal reproducibility.

References

1. Johnston, B.; Mayo, M.C.; Anshuman, K. Hydrogen: The energy source for the 21st century. *Technovation* **2005**, *25*, 569–585. [CrossRef]
2. Ali, A.; Pothu, R.; Siyal, S.; Phulpoto, D.; Sajjad, M.; Thebo, K. Graphene-based membranes for CO_2 separation. *Mater. Sci. Energy Technol.* **2019**, *2*, 83–88. [CrossRef]
3. Ameh, A.E.; Eze, C.P.; Antunes, E.; Cornelius, M.-L.U.; Musyoka, N.; Petrik, L.F. Stability of fly ash-based BEA-zeolite in hot liquid phase. *Catal. Today* **2019**, *357*, 416–424. [CrossRef]
4. Prodinger, S.; Derewinski, M.A. Recent Progress to Understand and Improve Zeolite Stability in the Aqueous Medium. *Pet. Chem.* **2020**, *60*, 420–436. [CrossRef]
5. Yang, X.; Du, H.; Lin, Y.; Song, L.; Zhang, Y.; Gao, X.; Kong, C.; Chen, L. Hybrid organosilica membrane with high CO2 permselectivity fabricated by a two-step hot coating method. *J. Membr. Sci.* **2016**, *506*, 31–37. [CrossRef]
6. Wei, Q.; Ding, Y.-L.; Nie, Z.-R.; Liu, X.-G.; Li, Q.-Y. Wettability, pore structure and performance of perfluorodecyl-modified silica membranes. *J. Membr. Sci.* **2014**, *466*, 114–122. [CrossRef]
7. Li, W.; Li, D.; Zheng, L.; Fan, J.; Zhang, Z. Preparation of Nickel-Doped Silica Films and Gas Separation Performance for CH_4/CO_2. *J. Chin. Ceram. Soc.* **2014**, *42*, 416–422.
8. Yang, J.; Xing, X.; Zhao, Y.; Mu, R.; Guo, Y.; Hou, H. Microstructures of nickel-doped methylated silica membrane materials calcined in air: Influence of Ni content. *Ferroelectrics* **2020**, *562*, 85–95. [CrossRef]
9. Yang, J.; Tian, L. Preparation, Characterization and Surface Free Energy of Nickel-Doped Silica Organic Inorganic Hybrid Membrane for H_2/CO_2 Separation. *J. Nanosci. Nanotechnol.* **2019**, *19*, 3180–3186. [CrossRef]
10. Lei, J.; Song, H.; Wei, Y.; Zhao, S.; Qi, H. A novel strategy to enhance hydrothermal stability of Pd-doped organosilica membrane for hydrogen separation. *Microporous Mesoporous Mater.* **2017**, *253*, 55–63. [CrossRef]
11. Gu, Y.; Zhong, S. Preparation and Application of Supported Palladium-Modified Polyimide-Silica Hybrid Membrane for Selective Separation of H_2. *Chin. J. Catal.* **2006**, *3*, 250–254.
12. Hove, M.; Nijmeijer, A.; Winnubst, L. Facile synthesis of zirconia doped hybrid organic inorganic silica membranes. *Sep. Purif. Technol.* **2015**, *147*, 372–378. [CrossRef]
13. Qi, H.; Han, J.; Xu, N. Effect of calcination temperature on carbon dioxide separation properties of a novel microporous hybrid silica membrane. *J. Membr. Sci.* **2011**, *382*, 231–237. [CrossRef]

14. Karakiliç, P.; Huiskes, C.; Luiten-Olieman, M.W.J.; Nijmeijer, A.; Winnubst, L. Sol-gel processed magnesium-doped silica membranes with improved H_2/CO_2 separation. *J. Membr. Sci.* **2017**, *543*, 195–201. [CrossRef]

15. Kanezashi, M.; Miyauchi, S.; Nagasawa, H.; Yoshioka, T.; Tsuru, T. Gas permeation properties through Al-doped organosilica membranes with controlled network size. *J. Membr. Sci.* **2014**, *466*, 246–252. [CrossRef]

16. Igi, R.; Yoshioka, T.; Ikuhara, Y.H.; Iwamoto, Y.; Tsuru, T. Characterization of Co-doped silica for improved hydrothermal stability and application to hydrogen separation membranes at high temperatures. *J. Am. Ceram. Soc.* **2008**, *91*, 2975–2981. [CrossRef]

17. Yang, J.; Ai, Y.; Fan, W.; Mu, R.; Chen, X.; Hou, H. Cobalt-Doped Silica Organic-Inorganic Materials by Sol-Gel Method: Preparation and Thermal Stability Calcined under N2 Atmosphere. *Integr. Ferroelectr.* **2021**, *219*, 247–259. [CrossRef]

18. Boffa, V.; Blank, D.; Elshof, J.E.T.; Tenelshof, J. Hydrothermal stability of microporous silica and niobia–Silica membranes. *J. Membr. Sci.* **2008**, *319*, 256–263. [CrossRef]

19. Lin, D.; Song, H.; Zhu, H.; Chen, J.; Qi, H. The influence of the particle size of polymer sol on the gas separation performance of niobium-doped organic-inorganic hybrid SiO_2 membrane. *Membr. Sci. Technol.* **2016**, *36*, 23–29.

20. Košutová, T.; Horák, L.; Pleskunov, P.; Hanuš, J.; Nikitin, D.; Kúš, P.; Cieslar, M.; Gordeev, I.; Burazer, S.; Choukourov, A.; et al. Thermally-driven morphogenesis of niobium nanoparticles as witnessed by in-situ x-ray scattering. *Mater. Chem. Phys.* **2021**, *277*, 125466. [CrossRef]

21. Frevel, L.K.; Rinn, H.W. Powder Diffraction Standards for Niobium Pentoxide and Tantalum Pentoxide. *Anal. Chem.* **1955**, *27*, 1329–1330. [CrossRef]

22. Brauer, G. Die oxyde des niobs. *Z. Anorg. Allg. Chem.* **1941**, *248*, 1–31. [CrossRef]

23. Kato, K.; Tamura, S. Die kristallstruktur von $T-Nb_2O_5$. *Acta Crystallogr. Sect. B Struct. Crystallogr. Cryst. Chem.* **1975**, *31*, 673–677. [CrossRef]

24. Angerer, P.; van Karsbergen, V.; Weinberger, N.; Strauss, G.; Neubauer, E.; Friessnegger, B.; Marsoner, S. In-situ high-temperature X-ray diffraction investigations of magnetron sputtered niobium oxide layers up to 900 °C. *Thin Solid Films* **2019**, *674*, 33–38. [CrossRef]

25. Francisco, M.; Gushikem, Y. Synthesis and characterization of $SiO_2–Nb_2O_5$ systems prepared by the sol–gel method: Structural stability studies. *J. Mater. Chem.* **2002**, *12*, 2552–2558. [CrossRef]

26. Boffa, V.; Elshof, J.E.T.; Petukhov, A.V.; Blank, D.H.A. Microporous Niobia–Silica Membrane with Very Low CO_2 Permeability. *ChemSusChem* **2008**, *1*, 437–443. [CrossRef]

27. Boffa, V.; Elshof, J.T.; Garcia, R.; Blank, D. Microporous niobia-silica membranes: Influence of sol composition and structure on gas transport properties. *Microporous Mesoporous Mater.* **2009**, *118*, 202–209. [CrossRef]

28. de Vos, R.M.; Verweij, H. Improved performance of silica membranes for gas separation. *J. Membr. Sci.* **1998**, *143*, 37–51. [CrossRef]

29. Nair, B.N.; Keizer, K.; Suematsu, H.; Suma, Y.; Kaneko, N.; Ono, S.; Okubo, A.T.; Nakao, S.-I. Synthesis of Gas and Vapor Molecular Sieving Silica Membranes and Analysis of Pore Size and Connectivity. *Langmuir* **2000**, *16*, 4558–4562. [CrossRef]

30. Uhlhorn, R.; Keizer, K.; Burggraaf, A. Gas transport and separation with ceramic membranes. Part II. Synthesis and separation properties of microporous membranes. *J. Membr. Sci.* **1992**, *66*, 271–287. [CrossRef]

31. Kanezashi, M.; Fujita, T.; Asaeda, M. Nickel-Doped Silica Membranes for Separation of Helium from Organic Gas Mixtures. *Sep. Sci. Technol.* **2005**, *40*, 225–238. [CrossRef]

32. Yoshida, K.; Hirano, Y.; Fujii, H.; Tsuru, T.; Asaeda, M. Hydrothermal Stability and Performance of Silica-Zirconia Membranes for Hydrogen Separation in Hydrothermal Conditions. *J. Chem. Eng. Jpn.* **2001**, *34*, 523–530. [CrossRef]

33. Qureshi, H.F.; Nijmeijer, A.; Winnubst, L. Influence of sol–gel process parameters on the micro-structure and performance of hybrid silica membranes. *J. Membr. Sci.* **2013**, *446*, 19–25. [CrossRef]

34. Song, H.; Zhao, S.; Lei, J.; Wang, C.; Qi, H. Pd-doped organosilica membrane with enhanced gas permeability and hydrothermal stability for gas separation. *J. Mater. Sci.* **2016**, *51*, 6275–6286. [CrossRef]

35. Wang, L.; Yang, J.; Mu, R.; Guo, Y.; Hou, H. Sol-Gel Processed Cobalt-Doped Methylated Silica Membranes Calcined under N_2 Atmosphere: Microstructure and Hydrogen Perm-Selectivity. *J. Mater.* **2021**, *14*, 4188. [CrossRef]